

Monte Carlo Physics-informed neural networks for multiscale heat conduction via phonon Boltzmann transport equation

Qingyi Lin^a, Chuang Zhang^b, Xuhui Meng^{a,1}, Zhaoli Guo^{a,1}

^a*Institute of Interdisciplinary Research for Mathematics and Applied Science, School of Mathematics and Statistics, Huazhong University of Science and Technology, Wuhan 430074, China*

^b*Department of Physics, School of Sciences, Hangzhou Dianzi University, Hangzhou 310018, China*

Abstract

The phonon Boltzmann transport equation (BTE) is widely used for the description of multiscale heat conduction (from nm to μm or mm) in solid materials. Developing numerical approaches to solve this equation is challenging since it is a 7-dimensional integral-differential equation. In this work, we propose the Monte Carlo physics-informed neural networks (MC-PINNs), which do not suffer from the “*curse of dimensionality*”, to solve the phonon Boltzmann transport equation for modeling the multiscale heat conduction in solid materials. In MC-PINNs, we utilize a deep neural network to approximate the solution to the BTE and encode the BTE as well as the corresponding boundary/initial conditions using the automatic differentiation. In addition, we propose a novel two-step sampling approach to address the issues of inefficiency and inaccuracy issues in the widely used sampling methods in PINNs. In particular, we first randomly sample a certain number of points in the temporal-spatial space (Step I) and then draw another number of points randomly in the solid angular space (Step II). The training points are constructed based on the data drawn from the above two steps using the tensor product. The two-step sampling strategy enables the MC-PINNs (1) to model the heat conduction from ballistic to diffusive regimes, and (2) is memory more efficient compared to the conventional numerical solvers or

¹Corresponding authors: xuhui_meng@hust.edu.cn (Xuhui Meng); zlguo@hust.edu.cn (Zhaoli Guo).

existing PINNs for BTE. A series of numerical examples including a quasi-one-dimensional (quasi-1D) steady/unsteady heat conduction in a film, and the heat conduction in a quasi-two- and three-dimensional square domain, are conducted to justify the effectiveness of the MC-PINN for heat conduction spanning diffusive and ballistic regimes. Finally, we perform a comparison of the computational time and the memory usage of the MC-PINN with one of the state-of-art numerical methods to demonstrate the potential of the MC-PINN for large-scale problems in real-world applications.

Keywords: phonon Boltzmann transport equation, physics-informed neural networks, two-step sampling approach, multiscale heat conduction

PACS: 0000, 1111

2000 MSC: 0000, 1111

1. Introduction

Microdevices, e.g., microprocessors and microelectronic circuits, often generate heat with great density during operation. Efficient thermal management is crucial to the reliability and optimal performance of these devices. As pointed out in [1], the heat conduction in microdevices like chips is inherently a multiscale problem spanning nanoscale (1-100 nm) to microscale (0.1-100 μm) or macroscopic (0.1-100 mm). The classical Fourier's law is a widely used empirical *macroscopic* model for heat conduction in solids. However, it is not capable of describing the heat conduction in the non-diffusive or ballistic regime [2, 3, 4]. Further, the phonon Boltzmann transport equation (BTE) is generally employed for describing the heat conduction in solid materials spanning the ballistic and diffusive regimes [5, 1, 6, 7].

To advance the understanding of multiscale heat conduction in solid materials, lots of efforts have been put into developing numerical methods for solving the phonon BTE. As mentioned, developing effective numerical methods for efficiently solving the phonon BTE is challenging since it is a 7-dimensional integral differential equation in real-world applications. The conventional numerical methods can be broadly categorized into two main approaches, i.e., the stochastic methods, e.g., direct simulation Monte Carlo (DSMC) [8, 9, 10, 11], etc., and deterministic approaches, e.g., discrete velocity/ordinate method [12, 13, 14], synthetic iterative scheme [15, 16, 17], discrete unified gas kinetic scheme (DUGKS) [18, 19], and so on. The former uses discrete meshes in the temporal-spatial space and is efficient for steady

problems in the ballistic regime. However, it converges slowly for problems in the (near) diffusive regime as well as non-stationary problems. The latter employs the discrete meshes in the temporal-spatial-angular space and is able to achieve good accuracy for steady/unsteady problems spanning a wide range of regimes. In general, the number of discrete points in the solid angular space required to obtain accurate results for the heat conduction problem in the diffusive regime is much smaller than in the ballistic regime. The requirement of large numbers of discrete points in the solid angular space for accurately capturing the non-Fourier’s behavior in the ballistic regime leads to intensive computational cost and prohibitive memory usage for large-scale thermal engineering problems in practice.

Deep neural networks (DNNs), which are able to break the curse of dimensionality, have recently emerged as an effective tool for solving partial differential equations (PDEs), such as physics-informed neural networks (PINNs) [20, 21, 22, 23] and DeepRitz [24]. Generally, the DNN-based PDE solvers are mesh-free, which saves significant effort for generating the meshes in conventional methods, e.g., finite volume method, and finite element method. Among the aforementioned deep learning approaches, the PINNs, which encode the PDEs via the automatic differentiation technique, are one of the most widely used methods for solving PDE problems due to their effectiveness and straightforward implementations. Recently, the PINNs have been successfully employed to simulate flows ranging from continuous to rarefied flows by solving the Boltzmann-BGK or Boltzmann equation, demonstrating their capability of handling multiscale problems [25, 26]. Inspired by the aforementioned work for modeling multiscale flows using PINNs, Li *et al.* proposed to solve the phonon BTE using PINNs to study the heat conduction in solid materials [27, 28]. The results show that the PINNs are capable of modeling heat conduction ranging from ballistic to diffusive regimes with satisfactory accuracy. In particular, the temporal-spatial, as well as the solid angular space, are discretized as a priori for training the PINNs in previous works [25, 27, 29]. For instance, the angular space is discretized utilizing the points in the Gauss Legendre quadrature rule, which is similar to the way widely used in the conventional deterministic approaches for solving phonon BTE, e.g., DUGKS. Although the effort of generating the meshes in temporal-spatial space can be saved for the PINN approaches, it shares the same defect as in the conventional deterministic approaches, i.e., a large number of discrete points in the phase space is required for heat conduction at the ballistic regime. Moreover, for scenarios in real-world ap-

plications where the heat conduction at the micro- and nanoscale coexists, a large number of discrete points in the phase space of phonon BTE is also required for accurate descriptions of the non-Fourier’s behavior at the ballistic regime since it is challenging to develop adaptive discretization for heat conduction at different scales. Therefore, we still have difficulty employing the PINNs for heat conduction in large-scale problems due to the expensive computational as well as memory cost. Numerical approaches for solving the phonon BTE that are more flexible as well as efficient are herein still desirable.

In this study, we employ the PINNs as the backbone to solve the phonon BTE due to their effectiveness and capability for handling high-dimensional problems. In particular, we propose a novel two-step sampling approach for the training of PINNs to address the issue of expensive computational and memory costs in the existing PINN models. We refer to the PINN equipped with the proposed two-step sampling approach as the Monte Carlo PINNs, which (1) is capable of modeling the heat conduction spanning ballistic to diffusive regimes, (2) is mesh-free in the temporal-spatial and the angular space, (3) is a unified approach at all regimes without the requirement to employ different discretizations in the angular space for heat conduction at different scales, and (4) requires much less discrete points in the angular space at each training step, and thus is more computationally and memory efficient comparing to the approach in [27].

The rest of the paper is organized as follows. In Sec. 2, we introduce the methodology, including the phonon BTE, and the PINN approach along with the two-step sampling strategy which is crucial for multiscale heat conduction. In Sec. 3, a series of numerical experiments are conducted, including steady and unsteady quasi-1D, quasi-2D, and 3D multiscale heat conduction problems. We finally summarize this study in Sec. 4.

2. Methodology

In this section, we first introduce the phonon Boltzmann transport equation as well as the corresponding boundary/initial conditions, which are used to describe the heat conduction from the ballistic to diffusive regime. We then present the MC-PINNs, i.e., physics-informed neural networks, and the proposed two-step sampling approach for the training of PINNs.

2.1. Phonon Boltzmann transport equation

The phonon Boltzmann transport equation (BTE) is a fundamental tool for understanding heat conduction in solid materials at different scales. Various models of the phonon BTE have been developed to address specific physical scenarios [9]. For instance, the full/linearized phonon BTE considers the detailed phonon dispersion and full scattering kernel, enabling the study of complex interactions among different phonon modes [30]. For scenarios that demand frequency-specific considerations, the frequency-resolved BTE under relaxation time approximation is often employed, in which the relaxation rate on the diagonal of phonon scattering matrix is accounted [10, 11, 16, 17]. A widely used model among these approaches is the gray model, where non-linear phonon dispersion and polarization are not accounted for and the frequency-independent assumption is used [19, 15, 17]. In this study, we focus on the phonon gray model, which is apt for probing multiscale heat conduction in three-dimensional materials subject to minor temperature variations, i.e., $\Delta T \ll T_{ref}$. Based on a certain number of reference variables, e.g., reference temperature T_{ref} , specific heat C_{ref} , reference length L_{ref} , group velocity v_g and time $t_{ref} = L_{ref}/v_g$, then the dimensionless phonon BTE in the gray model can be obtained as

$$\frac{\partial e''}{\partial t} + \mathbf{s} \cdot \nabla_{\mathbf{x}} e'' = \frac{1}{\text{Kn}} (e^{eq} - e''), \quad (1a)$$

$$e^{eq} = \frac{C_V T}{4\pi}, \quad (1b)$$

where e'' represents the phonon distribution function of energy density, which is a function of time t , spatial coordinate \mathbf{x} , and the unit directional vector $\mathbf{s} = (\cos \theta, \sin \theta \cos \varphi, \sin \theta \sin \varphi)$. Specifically, $\theta \in [0, \pi]$ and $\varphi \in [0, 2\pi]$ are the polar and azimuthal angles, respectively. In addition, e^{eq} denotes the equilibrium distribution function for the energy density; C_V and T are the specific heat and temperature, respectively. Moreover, $\text{Kn} = \lambda/L_{ref}$ is the Knudsen number defined as the ratio between the phonon mean free path to the characteristic length for a specific system. Due to the law of energy conservation, we can obtain the following equation for the right-hand side of Equation (1a):

$$0 = \int_{4\pi} \frac{e^{eq} - e''}{\text{Kn}} d\Omega, \quad (2)$$

where $d\Omega$ represents the integral over the entire solid angular space. The quantities of interest (QoI) in heat conduction problems including temperature T and heat flux \mathbf{q} can be obtained by taking the moment of phonon density distribution function, i.e.,

$$T = \frac{\int e'' d\Omega}{C_V}, \quad \mathbf{q} = \int \mathbf{s} e'' d\Omega. \quad (3)$$

We now introduce the boundary conditions briefly for solving Eq. (1), including the thermalization boundary condition, the periodic boundary condition, diffuse reflection, and so on. The periodic boundary condition, applied in repeated structures, ensures the continuity of the phonon flux and temperature field across opposite boundaries. Diffuse reflection conditions model rough surfaces, where phonons scatter in all directions based on the incoming distribution. In this work, we adopt the thermalization boundary condition for heat conduction problems [31], which allows us to simulate the heat conduction processes accurately for the boundary with a fixed temperature. Under this condition, phonons are absorbed upon striking the boundary, and new phonons are emitted with equilibrium states determined by the boundary temperature T_w . This is equivalent to implementing Dirichlet boundary conditions for the phonon energy density e'' at the boundary, with the rest derived from the governing equation:

$$e''(t, x_0, \mathbf{s}) = \frac{C_V T_w}{4\pi}, \quad \mathbf{s} \cdot \mathbf{n} > 0, \quad (4)$$

where \mathbf{n} is the unit normal vector pointing from the boundary to the computational domain. For the initial conditions, we assume that the distribution function is under equilibrium state at the initial temperature at $t = 0$:

$$e''(t_0, x, \mathbf{s}) = \frac{C_V T_0}{4\pi}. \quad (5)$$

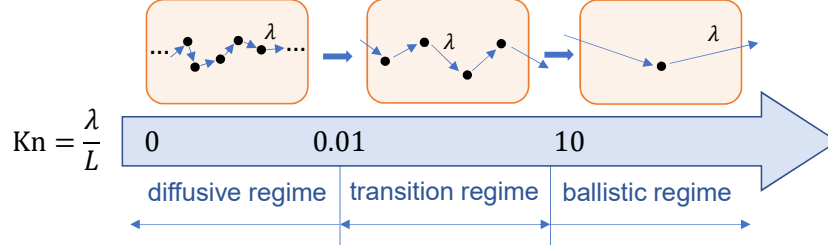


Figure 1: Schematic of flow regimes based on the Knudsen number. L is the characteristic length of the system and λ is the phonon mean free path.

We would like to discuss that the multiscale heat conduction is generally divided into different regimes based on the Knudsen number, seen in Figure 1. When $\text{Kn} < 0.01$, the characteristic length of the system is much larger than the phonon mean free path, and phonon transport is in the diffusive regime. The resulting temperature field is linear, consistent with the predictions of Fourier's law of heat conduction. As Kn increases, Fourier's law begins to fail. When $\text{Kn} > 10$, heat transfer is dominated by ballistic effects.

2.2. PINNs for phonon BTE

2.2.1. Physics-informed neural networks

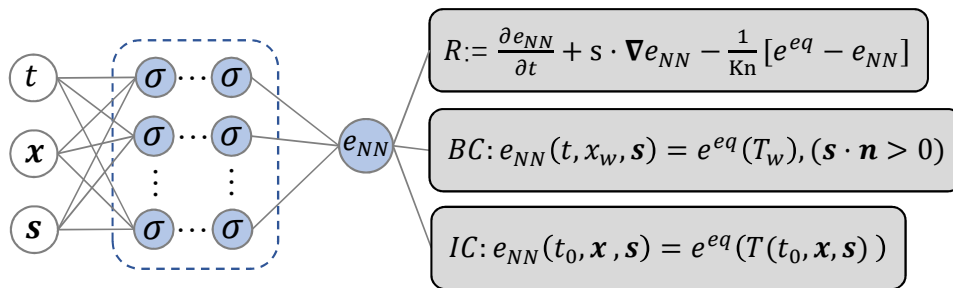


Figure 2: Schematic of physics-informed neural networks for phonon Boltzmann transport equation. $(t, \mathbf{x}, \mathbf{s})$ is the input, σ are the activation functions in the networks, and e_{NN} is the output of the neural networks. The gray boxes represent the physics-informed parts, i.e., the governing equation and boundary/initial conditions.

The PINNs for solving phonon BTE are illustrated in Fig. 2. As shown, we first utilize deep neural networks (DNNs), which take inputs as $(t, \mathbf{x}, \mathbf{s})$, to approximate the solution to Eq. (1), i.e., e'' , and then the governing equation, as well as the boundary and/or the initial conditions, are encoded in the DNNs via the automatic differentiation [32]. The loss function for training the PINNs is composed of the mean squared errors for the residual of the equation, mismatches between the predictions of DNNs and the boundary/initial conditions, which is expressed as follows:

$$L = L_{Eq} + L_{BC} + L_{IC}, \quad (6)$$

where L is the total loss, L_{Eq} , L_{BC} , and L_{IC} denote the losses corresponding to the loss of equation, boundary, and initial conditions, respectively. In addition, $L_{Eq}/L_{BC}/L_{IC}$ is computed following

$$\begin{aligned} L_{Eq} &= \frac{1}{N} \sum_{i=1}^N |R_i(t, \mathbf{x}, \mathbf{s})|^2, \\ L_{BC} &= \frac{1}{N_{BC}} \sum_{j=1}^{N_{BC}} |e_{NN,j}^{eq}(t, \mathbf{x}_w, \mathbf{s}) - e_j(t, \mathbf{x}_w, \mathbf{s})|^2, \\ L_{IC} &= \frac{1}{N_{IC}} \sum_{k=1}^{N_{IC}} |e_k^{eq}(t_0, \mathbf{x}, \mathbf{s}) - e_{NN,k}(t_0, \mathbf{x}, \mathbf{s})|^2, \end{aligned} \quad (7)$$

and

$$R = \partial_t e''_{NN} + \mathbf{s} \cdot \nabla e''_{NN} - \frac{1}{\text{Kn}} (e_{NN}^{eq} - e''_{NN}), \quad (8)$$

where R denotes the residual of the equation, and N , N_{BC} and N_{IC} are the numbers of training points used to compute the loss functions in PINNs for the residual, boundary, and initial conditions, respectively; R_i , $e_j^{eq}/e_{NN,j}$ and $e_k^{eq}/e_{NN,k}$ are quantities evaluated at points $(t, \mathbf{x}, \mathbf{s})_i$, $i = 1, \dots, N$, $(t, \mathbf{x}_w, \mathbf{s})_j$, $j = 1, \dots, N_{BC}$ and $(t_0, \mathbf{x}, \mathbf{s})_k$, $k = 1, \dots, N_{IC}$, respectively. In the present study, we refer to the points used to evaluate L_{Eq} , L_{BC} , and L_{IC} as residual, boundary, and initial points, respectively.

We note that the computations of the residual for the equation, i.e., R_i , require the calculation of the equilibrium energy density function, which is an integral defined in Eq. (2). Different approaches can be utilized to evaluate the integral since we can obtain the prediction of the energy density function at an arbitrary point $(t, \mathbf{x}, \mathbf{s})$ in the temporal-spatial-angular space via

the DNNs, e.g., Monte Carlo method, Gauss-Legendre, and Newton-Cotes quadrature. In the present study, it is found that Monte Carlo, which is computationally efficient at both low and high dimensions, is able to provide results with satisfactory accuracy. Hence, the Monte Carlo method is employed for the computations of e_{NN}^{eq} in this work.

As for the selection of the training points for evaluating the loss function in PINNs (Eq. (7)), two different ways are often used, i.e., (1) the number ($N/N_{BC}/N_{IC}$) as well as the locations of the training points are prescribed at each training step, and (2) the number of points ($N/N_{BC}/N_{IC}$) is prescribed, but the corresponding locations are randomly generated at each training step. The former is similar to the meshes in the conventional numerical methods. As mentioned, lots of discrete points in the solid angular space are required to accurately capture the non-Fourier behavior at the ballistic regime, which results in expensive computational and memory costs for multiscale heat conduction problems in real-world applications. For the latter approach, if we randomly generate training points in the temporal-spatial-angular domain, denoted as $(t, \mathbf{x}, \mathbf{s})_i, i = 1, \dots, M$, it is likely that each point $(t, \mathbf{x}, \mathbf{s})_i$ will be unique, meaning that for different i , the points $(t, \mathbf{x})_i$ correspond to different angular direction \mathbf{s}_i . As a result, during the training process, we only update the energy density function at each $(t, \mathbf{x})_i$ based on one single angular direction \mathbf{s}_i . It can lead to slow convergence or even degenerated results since we need to compute the integral in the entire angular domain, as we will show in Sec. 3.1.

2.2.2. Two-step sampling approach

To address the issues mentioned in the above two sampling methods, we propose the following two-step sampling strategy at each training step, i.e., (1) we first randomly draw $B_{t,\mathbf{x}}$ points in the temporal-spatial domain, i.e., $(t, \mathbf{x})_i, i = 1, \dots, B_{t,\mathbf{x}}$ (Step I); and (2) we then randomly draw $B_{\mathbf{s}}$ points in the solid angular domain, i.e., $\mathbf{s}_k, k = 1, \dots, B_{\mathbf{s}}$ (Step II). The training points in the temporal-spatial-angular space $(t, \mathbf{x}, \mathbf{s})$ at each training step are constructed using the tensor product given the points sampled at the two steps above. In general, we set $B_{\mathbf{s}} > 1$ to improve the accuracy for the computations of the integral in Eq. (2) as well as e^{eq} . Hence, we expect that the proposed two-step sampling approach is able to achieve better accuracy when compared to the second sampling method mentioned in Sec. 2.2.1. Note that for steady problems, we can just drop the dimension t , and perform the two-step sampling approach only in the spatial and angular domains, which

could improve the computational efficiency.

Here we further discuss the superiority of the two-step sampling approach over the the first sampling method in Sec. 2.2.1. As aforementioned, a large number of points in the solid angular domain has to be employed in the ballistic regime for the first approach of Sec. 2.2.1. In addition, how to determine the optimal number of discrete points at different regimes remains an open question. In the two-step sampling method, we randomly generate a certain number of points in the solid angular space at each training step. We can then traverse the entire angular domain even if we employ a small number of points in each step as long as we have enough training steps, which is similar to the statistic or particle methods for solving the BTE. Hence, compared to the discrete ordinate/velocity methods, the present solver is free of ray effects in the ballistic regime. Therefore, less computational and memory cost for heat conduction at the ballistic regimes are then expected at each training step if the two-step sampling strategy is adopted. Also, as we will show in Sec. 3.1, the two-step sampling method is more flexible than the first sampling approach in Sec. 2.2.1 for multiscale heat conduction problems. For the implementations of boundary/initial conditions, we can randomly generate a certain number of training points in the temporal-spatial-angular domain, i.e., $B_{t,x,s}$, since we do not need to compute the integral in boundary/initial conditions, for computational efficiency.

For the random sampling in solid angular space, as previously discussed, the group velocity of the distribution function in our phonon BTE model is uniformly distributed over the surface of a unit sphere. The points can then be expressed in the Cartesian coordinates as $(\cos \theta, \cos \theta \sin \phi, \sin \theta \sin \phi)$. In the present work, we first randomly sample the projection of the group velocity $\cos \theta \in [-1, 1]$ along the x -axis, and then sample the azimuthal angle $\phi \in [0, 2\pi]$ to generate the random points in the solid angular space.

3. Results and Discussion

In this section, we test the proposed method for simulating the heat conduction in solids ranging from diffusive to ballistic regimes, using four demonstration examples: (1) steady and unsteady quasi-one-dimensional (quasi-1D) film heat conduction, (2) quasi-two-dimensional (quasi-2D) heat conduction in a square domain, and (3) three-dimensional (3D) cuboid phonon transport. Further, the Adam optimizer, which is a variant of the stochastic gradient descent method, is utilized to minimize the loss functions in

MC-PINNs. The details for computations, e.g., the architectures of NNs, activation functions, and the numbers of training steps, etc., as well as the details for reference solutions, are present in Appendix A.

3.1. Quasi-1D film heat conduction

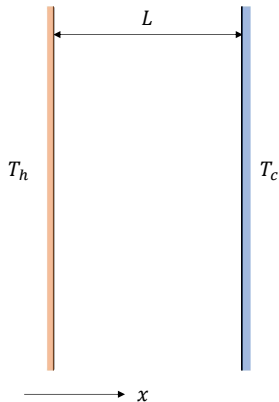


Figure 3: Schematic of the quasi-1D film heat conduction problem. T_h and T_c are the temperatures at the left and right boundaries, respectively; and L is the thickness of the film.

We first consider a quasi-1D heat conduction problem across a film, as depicted in Fig. 3. The thickness of the film is $L = 1$, which serves as the characteristic length of the problem. The temperatures at the left and right boundaries, i.e., $x = 0$ and L , are $T_h = 1$ and $T_c = 0$, respectively. Specifically, we employ the MC-PINNs to model the heat conduction at four different Knudsen numbers, i.e., $\text{Kn} = 0.01, 0.1, 1$, and 10 , to justify the capability of the present method for multiscale heat conduction. In all test cases, we randomly select $B_{\mathbf{x}} = 40$ and $B_{\mathbf{s}} = 16$ points in the spatial and angular domain for the computations of the loss for the equation at each training step. For the quasi-1D problem, the angular variable can be expressed as $s_x = \cos\theta$. For the boundary conditions, we randomly select $B_{x_0, \mathbf{s}} = 50$ points in the solid angular space at the boundary $x = 0$ and $x = 1$ and apply the thermalization boundary condition in Eq. (5).

To justify the accuracy of the present method, we first present the energy distribution functions for the case with $\text{Kn} = 1$ at two representative locations, i.e., $x = 0$ and 0.5 , computed from the MC-PINNs in Fig. 4. As

shown, the results from the MC-PINNs agree well with numerical results in [19]. In addition, the temperature as well as the heat flux are quantities of interest (QoI) in heat conduction problems rather than the energy distribution functions. We then illustrate the predicted temperature and the heat flux for $x \in [0, 1]$ from MC-PINNs in Fig. 5. It is observed that: (1) all the results from the MC-PINNs are in good agreement with those in [16], (2) the temperature exhibits significant nonlinearities near the boundaries for the test cases with $\text{Kn} > 0.01$ (Fig. 5(a)), and (3) the heat flux q remains constant although the temperature is nonlinear for $\text{Kn} > 0.01$, which is clearly different from the widely used Fourier’s law (Fig. 5(b)). In other words, the heat conduction for cases with $\text{Kn} > 0.01$ exhibits significant non-Fourier behavior.

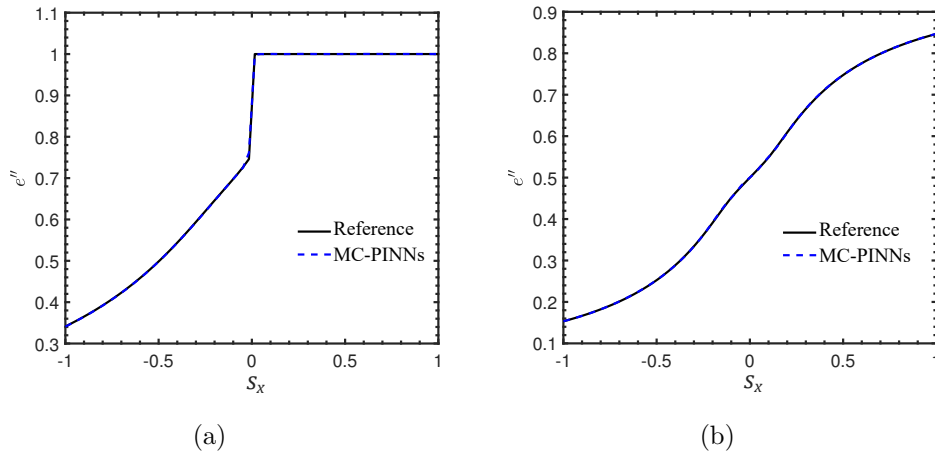


Figure 4: Quasi-1D film heat conduction: Predicted energy distribution function from MC-PINNs at $\text{Kn} = 1$ for (a) $x = 0$, and (b) $x = 0.5$. Black solid line: Reference solution [19]; Blue dashed line: MC-PINNs.

To further demonstrate the accuracy of the present method, we display the relative L_2 errors between the predicted temperature and heat flux from MC-PINNs and the reference solutions[19] in Table 1, where the relative L_2 error is computed as follows:

$$E_\phi = \frac{\|\phi_{ref} - \phi_{PINNs}\|_2}{\|\phi_{ref}\|_2}, \quad \phi = T, q. \quad (9)$$

As shown, the relative L_2 errors between the present method and the reference solutions for all test cases are less than 1%, demonstrating that the

MC-PINNs is capable of simulating heat conduction at both diffusive and ballistic scales with good accuracy.

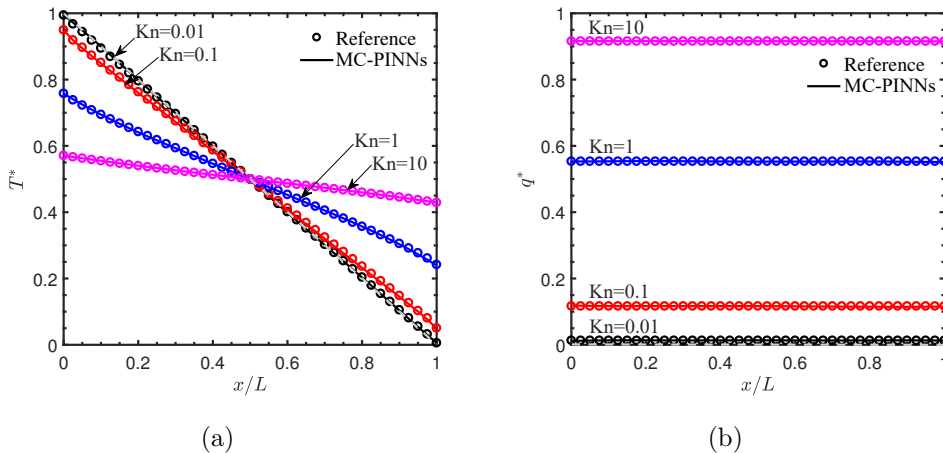


Figure 5: Quasi-1D film heat conduction: Predicted (a) temperature, and (b) heat flux, from MC-PINNs at different Knudsen numbers. Solid line: MC-PINNs; Symbols: Reference solution [16]. Gray dashed line: the solution of Fourier’s Law.

Table 1: Quasi-1D film heat conduction: Relative L_2 errors between PINNs and reference solution at different Kn. E_ϕ : Relative L_2 errors for temperature/heat flux.

-	Kn = 0.01	Kn = 0.1	Kn = 1	Kn = 10
E_T	0.515%	0.107%	0.052%	0.142%
E_q	1.000%	0.162%	0.090%	0.743%

As mentioned, the selection of training points in the solid angular space is crucial for the simulations of multiscale heat conduction. We now study the effect of different sampling approaches in the angular space on the predicted accuracy. Specifically, we test the following five different sampling approaches to obtain the residual points for training the PINNs:

1. **PINNs-1:** The two-step sampling proposed in the present study: we randomly sample B_x points in the spatial domain and B_s points in the solid angular domain, and then use a tensor product to generate the residual points at each training step.

2. **PINNs-2:** We employ B_x and B_s uniform discrete points in the spatial and solid angular domains, respectively.
3. **PINNs-3:** In the spatial domain, we use B_x uniform discrete points, and B_x quadrature points from the Gauss-Legendre method are employed in the solid angular domain, The residual points at each training step is then constructed using the tensor product. We note that this sampling approach is the same as in [27].
4. **PINNs-4:** We randomly sample B_s points in the solid angular domain, but use B_x uniform points in the spatial domain. Note that the sampling approach here can be viewed as a special case in PINN-1 by replacing the random points with the fixed uniform grids in the spatial domain.
5. **PINNs-5:** Randomly sample $B_x \times B_s$ residual points in the spatial-angular domain at each training step. We note that this approach is one of the most widely used methods in PINNs.

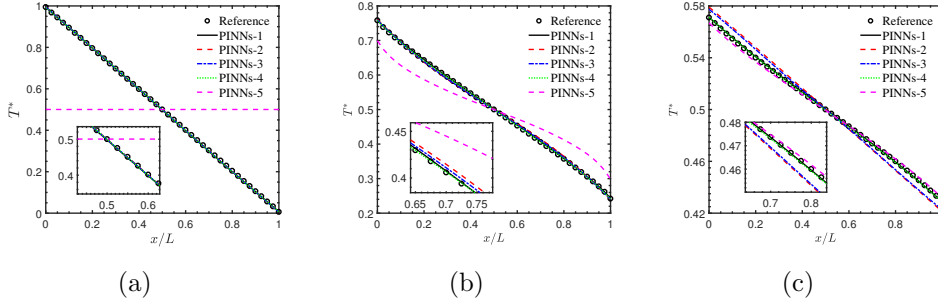


Figure 6: Quasi-1D film heat conduction: Effect of different sampling approaches in solid angular space on the predicted accuracy at (a) $\text{Kn} = 0.01$, (b) $\text{Kn} = 1$, and (c) $\text{Kn} = 10$. Symbols: Reference solution; PINNs-1: Two-step sampling method: Random sampling in both spatial and solid angular domain; PINNs-2: uniform discrete points in both spatial and solid angular domain; PINNs-3: uniform discrete points in spatial domain and GL quadrature points in angular domain; PINNs-4: Two-step sampling method: uniform discrete points in spatial domain and random sampling in solid angular space; PINNs-5: random sampling in spatial-angular domain.

We utilize these five sampling methods in PINNs to model the heat conduction in the 1D film at $\text{Kn} = 0.01, 1, \text{ and } 10$. The training step is set as 50,000 at $\text{Kn} = 1, 10$ and 10,0000 at $\text{Kn} = 0.01$ in all test cases. The results and the computational errors are present in Fig. 6 and Table 2, respectively. As we can see, (1) PINNs with the two-step sampling approach,

i.e., PINNs-1 and PINN-4, are able to provide the most accurate results for the heat conduction from diffusive to ballistic regimes; (2) the method in [27], i.e., PINNs-3, is able to achieve good accuracy for $\text{Kn} = 0.01$ and 1, but failed to capture the non-Fourier’s behavior accurately at $\text{Kn} = 10$ (e.g., the temperature jumps at the boundaries), as shown in Fig. 6(c); and (3) the computational errors for PINN-5 increases with the decreasing Kn . As discussed in Sec. 2.2.2, we only solve the BTE at one point in the solid angular space at each spatial point, leading to poor accuracy for the computation of e^{e^q} . At the ballistic scale, i.e., cases with large Kn , we have very few collisions for the phonon, and the inaccurate estimation of e^{e^q} has little effect on the predicted accuracy. However, for cases with small Kn , we have frequent collisions of the phonon, and the inaccurate prediction of e^{e^q} results in poor accuracy for solving the BTE.

Table 2: Quasi-1D film heat conduction: Relative L_2 errors of the temperatures between PINNs and reference solution with different training points. PINN-1 and PINN-4: Two-step sampling approach proposed in the current study; PINN-3: sampling approach used in [25, 27]; PINN-5: sampling approach used in [26].

-	PINNs-1	PINNs-2	PINNs-3	PINNs-4	PINNs-5
$E_T(\text{Kn} = 0.01)$	0.402%	0.383%	0.370%	0.390%	50.10%
$E_T(\text{Kn} = 1)$	0.299%	1.005%	0.678%	0.214%	9.201%
$E_T(\text{Kn} = 10)$	0.106%	1.280%	1.076%	0.130%	0.476%

3.2. Unsteady quasi-1D film heat conduction with varying Knudsen number

In this section, we apply our method to model the time-dependent heat conduction in a 1D film with a varying Knudsen number, which is defined as follows:

$$\text{Kn}(x) = \frac{\text{Kn}_{\max} + \text{Kn}_{\min}}{2} - \frac{\text{Kn}_{\max} - \text{Kn}_{\min}}{2} \tanh\left(\frac{x - x_c}{2d}\right), \quad (10)$$

where Kn_{\max} and Kn_{\min} represent the maximum and minimum Knudsen number, respectively; $x_c = L/2$ is the center of the film with L denoting the thickness of the film, and $d = 0.01$ characterizes the thickness of the transition layer. In the present case, we set $\text{Kn}_{\max} = 10$ and $\text{Kn}_{\min} = 0.01$. The distribution of the Knudsen number within the film is shown in Fig. 7. It can be seen that we have a significant change in Kn near the center of the

film. The heat conduction at the left half is at the ballistic regime, which is at the diffusive regime on the right half of the film.

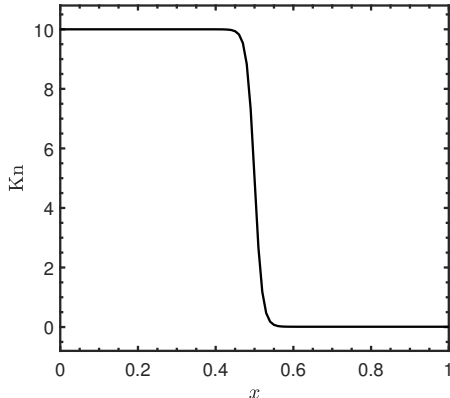


Figure 7: The varying Knudsen number within the film.

The computational domain as well as the boundary conditions are kept the same as in Sec. 3.1. In addition, we set $T(t = 0, \mathbf{x}) = (T_h + T_c)/2$ in the entire domain. The time domain here is set as $t \in [0, 10]$. In the computations, we sample $B_{t,x} = 100$ random points in the temporal-spatial domain and $B_s = 16$ random points in the solid angular domain. Further, $B_{t,x_0,s} = 100$ random points are sampled for boundary conditions and $B_{t_0,x,s} = 100$ random points for initial conditions.

Figure 8 presents the results obtained from the MC-PINNs at four representative times: $t = 0.2, 0.5, 1,$ and 10 . As shown, the results from the MC-PINNs show little differences with the reference solutions [19] at different times, demonstrating the good accuracy of the MC-PINNs for modeling multiscale heat conduction.

We would like to point out that 100 Gauss-Legendre quadrature points are employed in the solid angular space in the numerical method to accurately capture the non-Fourier's behavior [19]. In MC-PINNs, we only use 16 points in the solid angular domain at each training step, and it is capable of providing good results for heat conduction ranging from diffusive to ballistic scales. The above results indicate the great flexibility of the MC-PINNs with the two-step sampling approach. We do not need to carefully design the discretization of the angular domain, which is a long-standing challenge in conventional numerical methods for simulating multiscale heat conduction

problems.

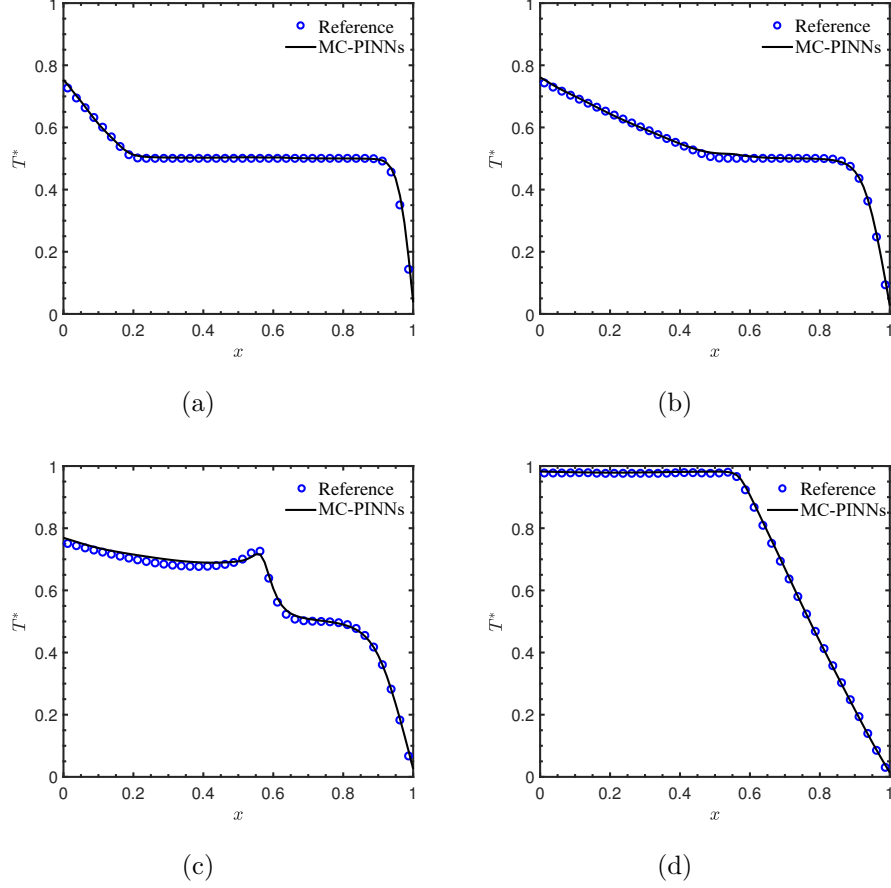


Figure 8: Unsteady quasi-1D film heat conduction: The predicted temperature at different times with space varying Knudsen number. (a) $t = 0.2$, (b) $t = 0.5$, (c) $t = 1.0$, (d) $t = 10.0$. Symbols: Reference solution [19]; Black solid line: MC-PINNs.

3.3. Quasi-2D square heat conduction

We now consider a quasi-2D heat conduction problem in a square domain with the length $L = 1$. The temperature is set to $T_h = 1$ at the top boundary and $T_c = 0$ at the remaining boundaries, as shown in Fig. 9. For the quasi-2D problem, the angular variable $\mathbf{s} = (s_x, s_y)$ can be expressed as follows:

$$s_x = \cos \theta, \quad s_y = \sin \theta \cos \phi, \quad (11)$$

where $\theta \in [0, \pi]$ and $\phi \in [0, \pi]$.

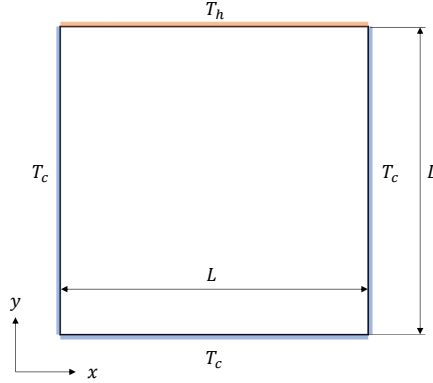


Figure 9: Schematic of the quasi-2D heat conduction in a square domain. L is the characteristic length, T_h is the upper plate non-dimensional temperature and T_c is the non-dimensional temperature of the remaining plates.

In this section, we employ the MC-PINNs to model the heat conduction in the 2D square domain at $\text{Kn} = 0.1, 1$ and 10 . In our computations, we first randomly sample $B_{\mathbf{x}} = 100$ points in the spatial domain and then select $B_{\mathbf{s}} = 64$ random points in the solid angular domain. As for boundary conditions, we randomly select $B_{\mathbf{x},\mathbf{s}} = 100$ in the spatial-angular domain at each boundary to implement the thermalization boundary condition defined in Eq. (5).

The results of MC-PINNs are shown in Figs. 10 and 11. We can see that the predicted temperatures from the MC-PINNs are in good agreement with the reference solutions in all test cases. We also observe in Figs. 10 and 11 there are significant temperature jumps at the left/right boundaries. In addition, the temperature jump becomes more pronounced with the increase of Kn . This phenomenon is reasonable since the non-equilibrium effects become more pronounced in the transition and ballistic regimes, leading to distinct temperature discontinuities at the walls.

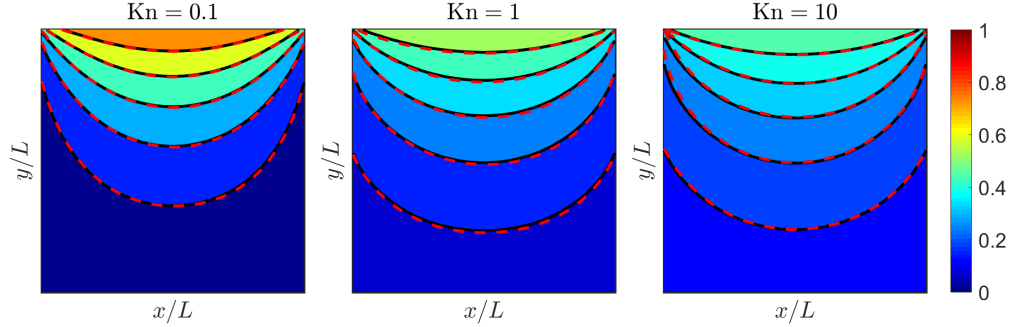


Figure 10: Quasi-2D heat conduction: Distribution of the temperature at (a) $\text{Kn} = 0.1$, (b) $\text{Kn} = 1.0$ and (c) $\text{Kn} = 10.0$. Colored background with black solid line: reference solution [17]; Red dashed line: the MC-PINNs.

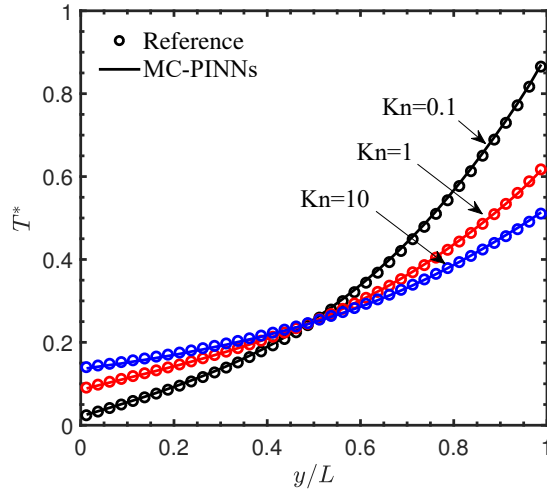


Figure 11: Quasi-2D heat conduction: Temperature along the center vertical line at different Kn . Solid line: MC-PINNs; Symbols: Reference solution [17].

We further compute the relative L_2 error between the MC-PINNs and the reference solutions at different Kn to demonstrate the accuracy of the present method in quasi-2D problems. As shown in Table 3, the relative L_2 errors for the three test cases are smaller than 2%, which again confirms the good accuracy of MC-PINNs for modeling multiscale heat conduction.

Table 3: Quasi-2D heat conduction problem: Relative L_2 errors between PINNs and reference solution at different Kn.

-	Kn = 0.1	Kn = 1.0	Kn = 10.0
E_T	1.55%	0.62%	1.21%

3.4. 3D cuboid phonon transport

In this section, we proceed to consider the phonon transport in a 3D cuboid. The temperature is set as T_h at the top boundary and T_c at the remaining boundaries, as shown in Fig. 12. Specifically, we set $T_h = 1$, $T_c = 0$, and $L = 1$. For the 3D problem, we have $\mathbf{s} = (s_x, s_y, s_z)$. Since the magnitude of the direction vector $|\mathbf{s}| = 1$, \mathbf{s} can then be expressed by θ and ϕ , i.e.,

$$\begin{aligned} s_x &= \cos \theta, \\ s_y &= \sin \theta \cos \phi, \\ s_z &= \sin \theta \sin \phi, \end{aligned} \tag{12}$$

where $\theta \in [0, \pi]$ and $\phi \in [0, 2\pi]$. In addition, we test the heat conduction at three representative Kn, i.e., Kn = 0.1, 1, and 10.

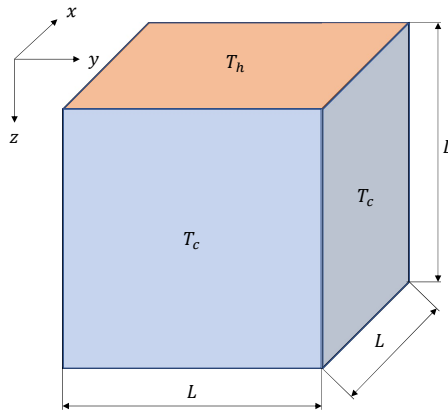


Figure 12: Schematic of the three-dimensional heat conduction in a cuboid.

In the MC-PINNs, the two-step sampling strategy is applied for generating the training points for the loss of residual with $B_x = 100$ and $B_s = 64$. For the boundary conditions, we randomly select $B_{\mathbf{x},\mathbf{s}} = 100$ in the spatial-angular domain for each wall at each training step. The boundary condition

implemented here is defined in Eq. (5), which is the same as the previous two cases in Secs. 3.1 and 3.3. As for the reference solution, we employ the implicit kinetic scheme to solve the stationary phonon BTE developed in [17]. We note that the numerical method in [17] employs a macroscopic equation to accelerate convergence in the diffusive regime. Additionally, it incorporates a memory reduction technique to reduce memory usage in computations. In numerical method the grid size is set to $40^3 \times 40^2$ at $\text{Kn} = 0.1, 1$ and $40^3 \times 80^2$ at $\text{Kn} = 10$ to ensure accuracy.

The predicted temperature from MC-PINNs in each case at $x = 0.5$ are present in Figs. 13 and 14. Again, good agreements are observed for all test cases between the MC-PINNs and the reference solutions. Similar to in the 2D cases, there are significant temperature jumps at the boundaries when $\text{Kn} \geq 1$, which have been discussed in Sec. 3.3 and will not present here for simplicity. We then illustrate the relative L_2 errors between the temperature from the MC-PINNs and the reference solutions at different Kn in Table 4. The results further confirm the capability of the MC-PINNs for 3D multiscale heat conduction problems.

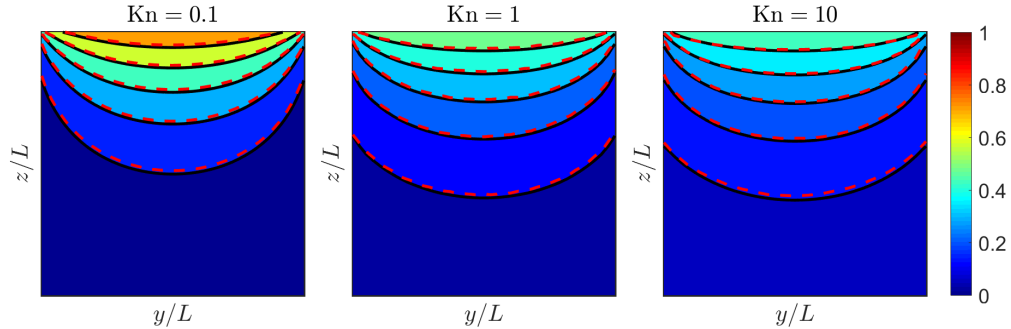


Figure 13: 3D heat conduction problem: Predicted temperature from MC-PINNs at $x = 0.5$ for different Kn . Colored background with black solid line: reference solution; Red dashed line: the MC-PINNs.

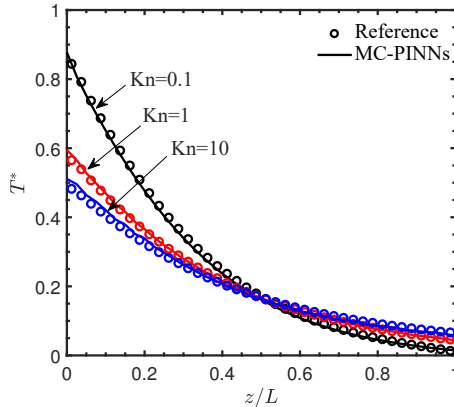


Figure 14: 3D heat conduction problem: Predicted temperature from MC-PINNs at $x = 0.5, y = 0.5$. Solid line: MC-PINNs; Symbols: Reference solution [17].

Table 4: 3D heat conduction problem: Relative L_2 errors between the temperature from MC-PINNs and reference solution at different Kn.

-	Kn = 0.1	Kn = 1.0	Kn = 10.0
E_T	2.49%	1.29%	1.91%

As mentioned, the method in [17] is one of the most computationally and memory-efficient approaches for solving stationary BTE. We now perform a comparison of the computational and the memory cost between the MC-PINNs and the numerical method [17] that is used to generate the reference solution here. Specifically, we compare the computational time and the memory usage using two representative cases, i.e., $\text{Kn} = 0.1$ and 10.

We first discuss the computational time for MC-PINNs. As illustrated in Table 5, the computational time of MC-PINNs (second column in Table 5) is about 7 and 1.3 times that in the numerical method [17] for $\text{Kn} = 0.1$ and 10, respectively. In the deep learning community, the transfer learning technique is a widely used approach to speed up the training of DNNs. Here we can also use it to speedup the training of MC-PINNs. Specifically, we first train the MC-PINNs from scratch for $\text{Kn} = 1$, and then save the hyperparameters, i.e., weights and biases, in order to reuse them in other cases. In particular, we initialize the MC-PINNs for $\text{Kn} = 0.1$ and 10 using the hyperparameters from the pre-trained MC-PINNs for $\text{Kn} = 1$ and further train them for an additional number of steps until the convergence is reached. The relative L_2

errors for these two cases with transfer learning are 2.40% and 2.6%, which are similar to the cases without transfer learning. Also, as we can see in Table 5, we can achieve about 3-6 times speedup with transfer learning, and the computational times for these two cases are now comparable to the numerical method in [17].

Note that we run the numerical method and MC-PINNs on the CPU and GPU, respectively. In particular, all the CPU computations are conducted on a single Intel Xeon Platinum 9242 processor, and the GPU computations are performed using an NVIDIA GeForce RTX 3090. We remark that the comparison present in Table 5 is not fair since we can also accelerate the numerical method by developing GPU codes and running the tests on GPUs. However, developing GPU codes for the numerical method is more challenging than MC-PINNs and is beyond the scope of the current study. We show the results here to provide a preliminary reference on the computational cost of MC-PINNs and one of the state-of-the-art numerical methods in this field. Therefore, we only present the computational time for the numerical method on CPUs.

Table 5: Computation time for the 3D heat conduction problem at $Kn = 0.1$ and 10 . First column: Numerical method on a single Intel Xeon Platinum 9242 processor. Second and third columns: MC-PINNs w/o and w/ transfer learning (TL). The MC-PINNs are run on one NVIDIA GeForce RTX 3090.

Kn	Numerical method	MC-PINNs (w/o TL)	MC-PINNs (w/ TL)
0.1	458s	3386s	870s
10	2500s	3101s	445s

We now discuss the memory usage for MC-PINNs and the numerical method, which is present in Table 6. Note that the MC-PINNs with and without transfer learning have the same memory cost. We therefore only illustrate the memory usage in the MC-PINNs without transfer learning in Table 6. In the MC-PINNs, we employ the same number of training points for $Kn = 0.1$ and 10 , and thus the memory usage is almost the same for these two cases. In the numerical method, the memory cost is more expensive for $Kn = 10$ than for $Kn = 0.1$ since we have more discrete points in the angular domain for the former case. Also, the MC-PINN requires about 66% and 16% of the memory cost in the numerical method [17] for $Kn = 0.1$ and 10 , respectively. It is worth mentioning that the problem we consider here is relatively small. For real-world applications, we may have more than 40

meshes in each direction of the spatial domain in numerical methods. For example, if we increase the number of meshes in each direction from 40 to 400 and keep the same discretization in the solid angular space for $\text{Kn} = 10$, the memory usage will increase to about 1,500GB, which is quite challenging to handle. However, in the MC-PINNs, we can use the same setup as used in the present case, suggesting that the memory usage can be the same, i.e., which is about 6,000 times less than in the numerical method [17].

Table 6: Memory usage for the 3D heat conduction problem at $\text{Kn} = 0.1$ and $\text{Kn} = 10$.

	$\text{Kn} = 0.1$	$\text{Kn} = 10$
Numerical method	381MB	1562MB
MC-PINNs	252MB	257MB

We would like to briefly summarize our main findings here: (1) the two-step sampling approach enables the MC-PINNs to use much less memory compared to the numerical method [17], especially for large-scale heat conduction problems spanning the diffusive and ballistic regimes; and (2) the computational time of MC-PINNs (GPU time) with transfer learning is comparable to the numerical method [17] (CPU time) for the specific problem considered here.

4. Summary

In this study, we develop a Monte Carlo physics-informed neural networks (MC-PINNs) for solving the phonon Boltzmann transport equation (BTE) to model the multiscale heat conduction in solid materials. Specifically, we utilize a deep neural network to approximate the energy density function in BTE and encode the BTE as well as the boundary/initial conditions via the automatic differentiation, in MC-PINNs. In addition, we propose a novel two-step sampling approach to address the issues like “curse of dimensionality” and the inaccurate estimate of the equilibrium distribution functions in the existing sampling strategies that are widely used in PINNs. In particular, we first randomly sample a certain number of points in the temporal-spatial domains (Step I), and then we draw another number of random points in the solid angular domain (Step II). The residual points in MC-PINNs are constructed using the tensor product given the points generated at the above two steps. We conduct a series of numerical experiments to validate the accuracy

of the MC-PINNs, including the steady quasi-1D/quasi-2D/3D as well as unsteady quasi-1D heat conduction problems spanning the diffusive and ballistic regimes. The results show the MC-PINNs is capable of achieving good accuracy for the multiscale heat conduction from 1D to 3D. Furthermore, the present method requires quite a small number of discrete points in the solid angular domain than in the deterministic methods for solving the BTE, especially for scenarios in the ballistic regimes. For instance, we only employ 64 points in the solid angular domain at each training step in MC-PINNs for Kn ranging from 0.1 to 10 in the 3D case. In contrast, we have 80×80 discrete points in the solid angular domain of the numerical method to obtain converged results. As a result, the memory cost in the MC-PINN is about 1/6 of that in the numerical method. Further, we are able to achieve a similar computational efficiency for MC-PINNs to the numerical method in the 3D test case as we utilize the transfer learning technique in the MC-PINNs.

We would like to discuss that the MC-PINN developed in this work is mesh-free in the temporal-spatial-angular domain, which is promising in real-world applications with complicated domains, for instance, the design of microdevices. In addition, the MC-PINN is capable of providing good accuracy for heat conduction ranging from diffusive to ballistic with only a small number of random discrete points in the solid angular domain at each training step. It can save lots of effort in numerical methods since the optimal discretization of the solid angular space at different regimes is generally different and should be carefully designed to ensure convergence in these methods. Also, the memory efficacy and the flexibility of treatment for the solid angular space in the present method make it a promising tool for modeling multiscale heat conduction in large-scale problems. Finally, we note that the MC-PINNs with the two-step sampling approach can be seamlessly extended to solve kinetic equations used in other disciplines, e.g., the Boltzmann-BGK model for multiscale flows, the radiation transfer equation for multiscale heat transfer, etc. We will leave these interesting topics as future studies.

Acknowledgement

QL, XM, and ZG acknowledge the support of the National Natural Science Foundation of China (No. 12201229) and the Interdisciplinary Research Program of HUST (No. 2023JCYJ002 and 2024JCYJ003). CZ was supported by the National Natural Science Foundation of China (No. 12147122).

XM would also like to acknowledge the support of Xiaomi Young Talents Program. The authors acknowledge Beijng PARATERA Tech CO., Ltd. for the HPC resources.

Appendix A. Details on the computations

In all the test cases of Sec. 3, the Adam optimizer with a learning rate 10^{-3} is employed for the training of PINNs. More details on the architectures of MC-PINNs, etc., are present in Table A.7.

Table A.7: Architecture and training step for MC-PINNs in each case.

	Width \times Depth	Activation function	Training steps
Sec. 3.1	20×4	tanh	50,000/100,000
Sec. 3.2	30×4	tanh	100,000
Sec. 3.3	30×4	tanh	200,000
Sec. 3.4	30×5	tanh	200,000
Appendix A	20×4	tanh	50,000

The details of grids utilized in the numerical methods for generating the reference solutions are presented in Table A.8. Note that in all cases, the uniform grids are employed in the temporal and spatial domain. As for the solid angular domain, the Gauss-Legendre quadrature points are employed.

Table A.8: Grid size used in the numerical method for generating reference solutions in each case. For the 3D case in Sec. 3.4, we use 40×40 and 80×80 points in the solid angular domain for $\text{Kn} = 0.1/1$ and 10, respectively.

	time (t)	space (\boldsymbol{x})	solid angular domain (\boldsymbol{s})
Sec. 3.1	-	40	100
Sec. 3.2	1600	80	100
Sec. 3.3	-	40×40	40×40
Sec. 3.4	-	$40 \times 40 \times 40$	$40 \times 40, 80 \times 80$
Appendix A	-	40	100

Appendix B. Ablation study

To study the effect of the number of the points in the solid angular space at each training step on the predicted accuracy of MC-PINNs, we further conduct the following experiments based on two specific cases in Sec. 3.1, i.e., $\text{Kn} = 1$ and 10. In each case, we test 6 different numbers of the points in the solid angular space, i.e. $B_s = 2, 4, 8, 16, 32$ and 64 points at each training step. Also, we independently run MC-PINNs 5 times with different initializations for the hyperparameters to test the robustness of the MC-PINNs. The number of B_x is set to 40, which is consistent with the case in Sec. 3.1. The predicted temperature from MC-PINNs is depicted in Fig. B.15. It is observed that: (1) the computational errors in general decrease with the increase of B_s , and (2) the relative L_2 errors between the results from MC-PINNs and the reference solutions in each case are below 1% as $B_s > 2$. In other words, we are able to achieve good accuracy as we randomly sample more than 2 points in the solid angular domain at each training step in MC-PINNs for these two specific cases.

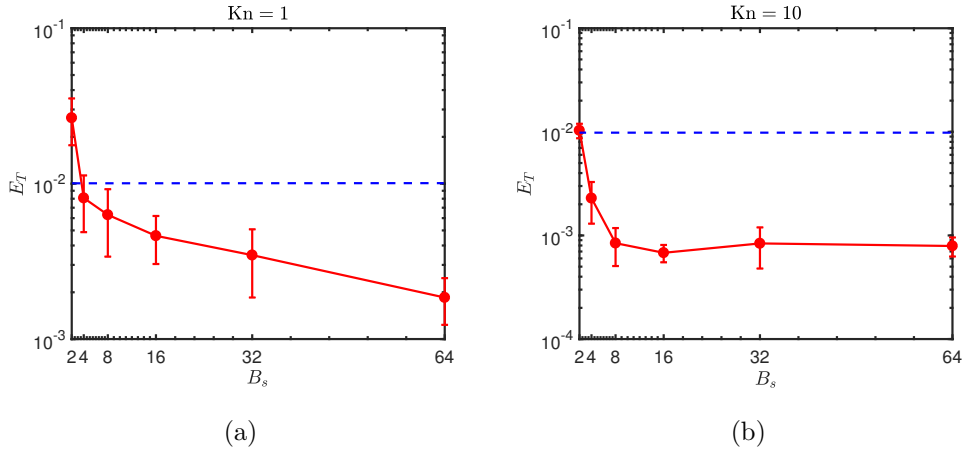


Figure B.15: Quasi-1D film heat conduction: Relative L_2 errors of the temperature with different numbers of points in the solid angular space at each training step in PINNs. (a) $\text{Kn} = 1$, and (b) $\text{Kn} = 10$. Error bars in each figure represent the standard deviation calculated from 5 independent runs with different random seeds. The blue dashed line denotes the relative L_2 error for 1%.

We further present the loss histories for the representative case $\text{Kn} = 1.0$ with $B_s = 2$ and 16 in Fig. B.16. As shown, the loss for MC-PINNs with

16 random points in the solid angular space after 50,000 training steps is about two orders smaller than that with 2 random points in the solid angular domain. Also, the fluctuations in the loss are smaller for the case with a larger number of points in the solid angular space at each training step.

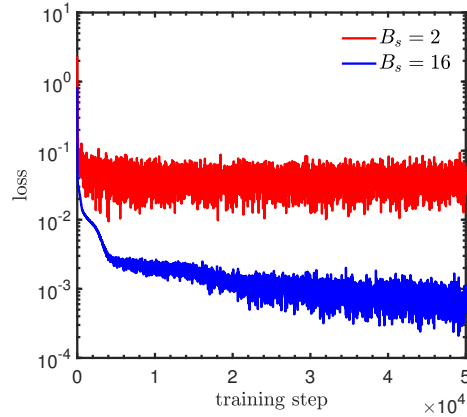


Figure B.16: Loss history for $B_s = 2$ and $B_s = 16$ at $\text{Kn} = 1.0$.

References

- [1] M. A. Stettler, S. M. Cea, S. Hasan, L. Jiang, P. H. Keys, C. D. Landon, P. Marepalli, D. Pantuso, C. E. Weber, Industrial lead: modeling atoms to chips, *IEEE Transactions on Electron Devices* 68 (11) (2021) 5350–5357.
- [2] G. Chen, Non-fourier phonon heat conduction at the microscale and nanoscale, *Nature Reviews Physics* 3 (8) (2021) 555–569.
- [3] Z. M. Zhang, Z. M. Zhang, Luby, *Nano/microscale heat transfer*, Vol. 410, Springer, 2007.
- [4] D. G. Cahill, P. V. Braun, G. Chen, D. R. Clarke, S. Fan, K. E. Goodson, P. Keblinski, W. P. King, G. D. Mahan, A. Majumdar, et al., *Nanoscale thermal transport. ii. 2003–2012*, *Applied Physics Reviews* 1 (1) (2014).
- [5] X. Chang, H. Oprins, M. Lofrano, V. Cherman, B. Vermeersch, J. D. Fortuny, S. Park, Z. Tokei, I. De Wolf, *Calibrated fast thermal calculation and experimental characterization of advanced beol*

- stacks, in: 2023 IEEE International Interconnect Technology Conference (IITC) and IEEE Materials for Advanced Metallization Conference (MAM)(IITC/MAM), IEEE, 2023, pp. 1–3.
- [6] J. M. Ziman, *Electrons and phonons: the theory of transport phenomena in solids*, Oxford university press, 2001.
 - [7] J. Y. Murthy, S. V. Narumanchi, P.-G. Jose'A, T. Wang, C. Ni, S. R. Mathur, Review of multiscale simulation in submicron heat transfer, *International Journal for Multiscale Computational Engineering* 3 (1) (2005).
 - [8] J.-P. M. Péraud, N. G. Hadjiconstantinou, Efficient simulation of multidimensional phonon transport using energy-based variance-reduced monte carlo formulations, *Physical Review B—Condensed Matter and Materials Physics* 84 (20) (2011) 205331.
 - [9] S. Mazumder, A. Majumdar, Monte carlo study of phonon transport in solid thin films including dispersion and polarization, *J. Heat Transfer* 123 (4) (2001) 749–759.
 - [10] M.-S. Jeng, R. Yang, D. Song, G. Chen, Modeling the thermal conductivity and phonon transport in nanoparticle composites using monte carlo simulation, *Journal of Heat Transfer* 130 (4) (2008) 042410.
 - [11] D. Lacroix, K. Joulain, D. Lemonnier, Monte carlo transient phonon transport in silicon and germanium at nanoscales, *Physical Review B—Condensed Matter and Materials Physics* 72 (6) (2005) 064305.
 - [12] D. P. Sellan, J. Turney, A. J. McGaughey, C. H. Amon, Cross-plane phonon transport in thin films, *Journal of Applied Physics* 108 (11) (2010).
 - [13] A. Christensen, S. Graham, Multiscale lattice boltzmann modeling of phonon transport in crystalline semiconductor materials, *Numerical Heat Transfer, Part B: Fundamentals* 57 (2) (2010) 89–109.
 - [14] S. V. J. Narumanchi, J. Y. Murthy, C. H. Amon, Comparison of different phonon transport models for predicting heat conduction in silicon-on-insulator transistors, *Journal of Heat Transfer* 127 (7) (2005) 713–723.

- [15] C. Zhang, Z. Guo, S. Chen, Unified implicit kinetic scheme for steady multiscale heat transfer based on the phonon boltzmann transport equation, *Physical Review E* 96 (6) (2017) 063311.
- [16] C. Zhang, Z. Guo, S. Chen, An implicit kinetic scheme for multiscale heat transfer problem accounting for phonon dispersion and polarization, *International Journal of Heat and Mass Transfer* 130 (2019) 1366–1376.
- [17] C. Zhang, S. Huberman, X. Song, J. Zhao, S. Chen, L. Wu, Acceleration strategy of source iteration method for the stationary phonon boltzmann transport equation, *International Journal of Heat and Mass Transfer* 217 (2023) 124715.
- [18] Z. Guo, K. Xu, R. Wang, Discrete unified gas kinetic scheme for all knudsen number flows: Low-speed isothermal case, *Physical Review E—Statistical, Nonlinear, and Soft Matter Physics* 88 (3) (2013) 033305.
- [19] Z. Guo, K. Xu, Discrete unified gas kinetic scheme for multiscale heat transfer based on the phonon boltzmann transport equation, *International Journal of Heat and Mass Transfer* 102 (2016) 944–958.
- [20] M. Raissi, P. Perdikaris, G. E. Karniadakis, Physics-informed neural networks: A deep learning framework for solving forward and inverse problems involving nonlinear partial differential equations, *Journal of Computational Physics* 378 (2019) 686–707.
- [21] M. Raissi, A. Yazdani, G. E. Karniadakis, Hidden fluid mechanics: Learning velocity and pressure fields from flow visualizations, *Science* 367 (6481) (2020) 1026–1030.
- [22] L. Lu, R. Pestourie, W. Yao, Z. Wang, F. Verdugo, S. G. Johnson, Physics-informed neural networks with hard constraints for inverse design, *SIAM Journal on Scientific Computing* 43 (6) (2021) B1105–B1132.
- [23] S. Cuomo, V. S. Di Cola, F. Giampaolo, G. Rozza, M. Raissi, F. Piccialli, Scientific machine learning through physics-informed neural networks: Where we are and what’s next, *Journal of Scientific Computing* 92 (3) (2022) 88.

- [24] B. Yu, et al., The deep ritz method: a deep learning-based numerical algorithm for solving variational problems, *Communications in Mathematics and Statistics* 6 (1) (2018) 1–12.
- [25] Q. Lou, X. Meng, G. E. Karniadakis, Physics-informed neural networks for solving forward and inverse flow problems via the boltzmann-bgk formulation, *Journal of Computational Physics* 447 (2021) 110676.
- [26] S. Jin, Z. Ma, K. Wu, Asymptotic-preserving neural networks for multiscale time-dependent linear transport equations, *Journal of Scientific Computing* 94 (3) (2023) 57.
- [27] R. Li, E. Lee, T. Luo, Physics-informed neural networks for solving multiscale mode-resolved phonon boltzmann transport equation, *Materials Today Physics* 19 (2021) 100429.
- [28] R. Li, J.-X. Wang, E. Lee, T. Luo, Physics-informed deep learning for solving phonon boltzmann transport equation with large temperature non-equilibrium, *npj Computational Materials* 8 (1) (2022) 29.
- [29] Z. Li, Y. Wang, H. Liu, Z. Wang, B. Dong, Solving the boltzmann equation with a neural sparse representation, *SIAM Journal on Scientific Computing* 46 (2) (2024) C186–C215.
- [30] V. Chiloyan, S. Huberman, Z. Ding, J. Mendoza, A. A. Maznev, K. A. Nelson, G. Chen, Green’s functions of the boltzmann transport equation with the full scattering matrix for phonon nanoscale transport beyond the relaxation-time approximation, *Physical Review B* 104 (24) (2021) 245424.
- [31] M. J. Fryer, H. Struchtrup, Moment model and boundary conditions for energy transport in the phonon gas, *Continuum Mechanics and Thermodynamics* 26 (2014) 593–618.
- [32] A. G. Baydin, B. A. Pearlmutter, A. A. Radul, J. M. Siskind, Automatic differentiation in machine learning: a survey, *Journal of Machine Learning Research* 18 (153) (2018) 1–43.